The design of central column protection tiles for the TCV tokamak

R.A. Pitts, R. Chavan, J.-M. Moret
Centre de Recherches en Physique des Plasmas,
Association Euratom–Confédération Suisse,
École Polytechnique Fédérale de Lausanne,
Lausanne, Switzerland

Abstract. The large variety of plasma shapes produced in the TCV tokamak places unique demands on the plasma facing surfaces. In particular, the central column graphite armour tiles are solicited during the creation of all TCV plasmas and function as power handling surfaces for both limited and diverted discharges. The higher power flux densities accompanying the addition of electron cyclotron heating systems have necessitated a new, optimized, design for these tiles. The optimization process and the subsequent new tile design are described. A basic 'two point' model of the scrape-off layer plasma in conjunction with TCV equilibrium reconstructions and a simplified representation of the local magnetic field line geometry are used to impose simulated power flux densities onto a parametric toroidal tile contour. The thermo-mechanical response of the tile is then investigated via full 3-D finite element simulations accounting for the non-linear temperature dependence of the graphite thermal diffusivity and radiation from the tile surface. The final design choice is a compromise between the requirements for adequate power handling for a range of magnetic configurations, the need to protect against tile edge misalignment in the presence of grazing field line angles of incidence and the space restrictions imposed by vacuum vessel design.

1. Introduction

The issue of first wall protection is of outstanding importance for most aspects of modern tokamak operation. In recent years, graphite has become the most commonly used first wall material, with complete coverage of the internal vacuum vessel surfaces now increasingly popular [1, 2]. For the majority of large tokamaks currently in operation, the presence of closed divertor volumes with specific geometries necessarily restricts the range of possible magnetic equilibria. In turn, this leads to a more constrained design problem with respect to first wall protection elements since they can be tailored to meet the requirements of an essentially fixed magnetic geometry. In the case of the TCV tokamak [3], the plasma configuration can change radically, even from discharge to discharge, imposing a certain flexibility on first wall components which are frequently required to play the role of both limiter and divertor surfaces.

Throughout the first five years of TCV operation, the first wall components have been systematically improved and augmented based both on experience gained in operating a larger variety of plasma shapes and according to the requirements of the physics programme. The recent installation of the first third of a planned 4.5 MW ECRH system [4], together with the successful creation of highly elongated discharges [5], has imposed replacement of the poorly optimized and hitherto unchanged central column protection tiles. This article describes the design philosophy, procedure and final solution to this latest TCV first wall modification.

2. TCV equilibria and first wall protection

The magnetic equilibrium reconstructions shown in Fig. 1 demonstrate the capacity of TCV for the creation of a wide variety of plasma shapes. Both limited and diverted configurations are readily produced, the latter in the form of upper or lower single null (SNU, SNL) and double null (DN). At the time of writing, the highly elongated discharge ($\kappa = 2.58$, $I_p = 725$ kA) limited on the central column, shown in Fig. 1(b), represents the highest elongation ever produced in a tokamak with conventional aspect ratio [5].

The limited equilibrium ($\kappa = 1.3$, $I_p = 170$ kA) shown in Fig. 1(e) is one example of the low density target plasmas used for ECR experiments with second harmonic heating at 82.6 GHz [6]. Figure 1(c) illustrates the SNL diverted configuration ($\kappa = 1.65$, $I_p = 280$ kA) used extensively for edge physics

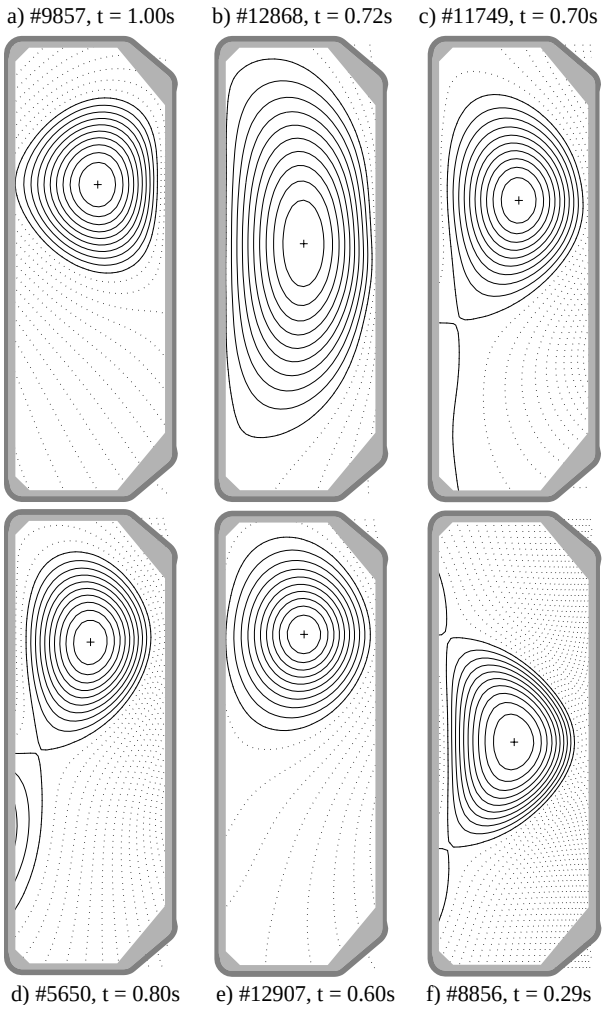

Figure 1. Illustration of the variety of magnetic equilibria already produced in TCV. The SNL diverted configuration in (c) and the limited equilibrium in (e) have been used extensively in designing the central column tiles.

studies. This discharge constitutes the TCV 'standard shot' and is executed at the beginning of every run day as a monitor of global recycling behaviour [7]. A variant of this configuration, the equilibrium in Fig. 1(d), has been used extensively for the study of ohmic H mode on TCV [8]. Geometries of this type are of particular importance in designing the new central column tiles as a consequence of both the rather localized heat deposition at the divertor strike points and the grazing angles at which magnetic field lines strike tile surfaces there.

The rather distinctive TCV rectangular vacuum vessel geometry ($R = 0.88$ m, with an internal height of 1.54 m and a width of 0.56 m (not including tiles)) is evident in the plasma cross-sections of Fig. 1. The vacuum vessel is a continuously welded structure, providing a passive shell for improved vertical stability at high elongation. Such passive stabilization is only effective, however, if plasma–wall distances are minimized, leading to tight constraints with regard to the space available for first wall components and in-vessel diagnostics, particularly at the central column on which the majority of plasmas thus far created depend for a limiter surface or divertor target.

During the first two years of TCV operation, graphite protection consisted of asymmetrically chamfered tiles for the central column, a set of tiles for the vessel floor, a toroidal belt limiter below the outside midplane and elsewhere individual tiles installed only for the protection of in-vessel poloidal magnetic field probes [9]. In 1993, new tile sets, optimized for diverted discharges (e.g. Fig. 1(c)), were added at the vessel floor and ceiling. Recently, the toroidal belt limiter was removed in favour of complete tiling of the low field side wall, leading to 90% graphite internal surface coverage and thus, essentially, an all-graphite first wall. This allows the range of possible equilibria to be extended and virtually eliminates plasma contamination by metallic impurities released from the previously exposed vacuum vessel surfaces. It was also hoped that the increased graphite coverage would permit good recycling control (in combination with regular helium glow discharge cleaning), particularly with respect to the low densities required for experiments with second harmonic ECRH. Experiments following the resumption of TCV operations after installation of the new tiles appear to confirm this qualitative expectation.

The original central column tiles were not specifically designed as limiting surfaces, being intended rather as protection for the stainless steel of the central cylinder and the in-vessel magnetic probes. The 'rooftop' design of these first tiles means that the plasma–surface interaction is strongly localized at the apex of each tile leading to inefficient power spreading at grazing magnetic field line incident angles. Although far from optimum, the design did not prevent satisfactory operation during the first years of experiments with ohmic discharges and hence relatively modest power flux densities.

3. Tile design concept and power flux model

The new central column tiles must satisfy a number of criteria determined by the requirements for adequate power handling, cost and mechanical

compatibility with the existing vacuum vessel. They are listed below with no particular attention paid to order of priority:

(a) Toroidal contour providing optimum power dispersal given the worst case field line angles of impact and radial power distribution in the SOL.

(b) Space restrictions preclude active cooling so that passive cooling between discharges must suffice at maximum power levels and pulse lengths (≈1 s).

(c) Adequate provision for shielding of leading edges for the worst case tile misalignment (given the restrictions of criterion 1).

(d) Symmetric toroidal contour allowing for arbitrary magnetic helicity, but no curvature in the poloidal direction to reduce tile complexity.

(e) As many identical units as possible to reduce cost and provide for easy replacement of failed units.

(f) Compatibility with existing distribution of rails and screw holes and provision of full protection for the extensive array of rail mounted, in-vessel magnetic field probes.

(g) Minimization of inter-tile gaps and provision of a mounting system hidden from direct plasma–surface interaction but compatibility with the limitations on tile thickness due to the requirement for small plasma–wall distances (passive stabilization).

3.1. Parametric tile contour

The requirements of criterion (c) above and the need for a limited number of degrees of freedom in the optimization of power dispersal lead naturally to specification of a segmented toroidal contour. Figure 2(a) illustrates the chosen tile structure, consisting of a curved front surface and an asymmetric back surface shaped to accommodate an in-vessel poloidal magnetic field probe. To satisfy criteria (e) and (f), all tiles retain this structure. The plasma facing surface (Fig. 2(b)) is defined by a cylindrical segment (TP_3) chamfered by elliptic edges (P_2P_3) such that the plasma facing contour is continuous in its derivative. Straight line segments (P_1P_2) join the elliptic sections to the tile base. The tile is symmetric about a line through the point T defining the maximum tile radius, $R_{tile}^{max} = 0.624$ m, fixed by the requirements of minimum plasma–wall separation for vertical stability.

Existing support rails welded on the vacuum vessel determine a toroidal periodicity of $\theta = 22.5°$ subtended by each pair of tiles, requiring 32 tiles to complete the central column circumference. In accordance with criterion (g), a nominal, minimum

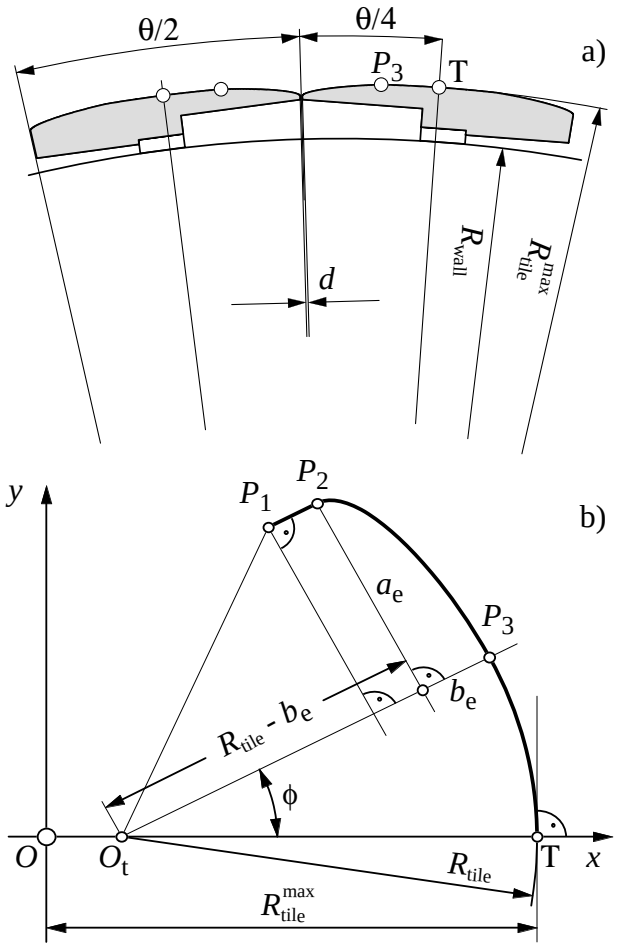

Figure 2. (a) Illustration of the basic structure of the 32 tiles required to complete the central column toroidal circumference. Note that the symmetric plasma facing contour and the rear surface are machined to house in-vessel poloidal magnetic field probes. (b) The parametric tile contour comprises a cylindrical central section flanked by elliptical end portions. O, torus axis.

inter-tile gap of $d = 1$ mm is imposed, subject to the presence of toroidal non-uniformities in the vacuum vessel itself. One may also note the importance of criterion (d) for the particular case of TCV in which equilibria such as those shown in Fig. 1(d) have opposite directions of poloidal field at the two divertor strike points and a consequent inversion in total field line attack angle from one target zone to the other.

Along with R_{tile}, the ellipse axes a_e and b_e constitute the three geometric parameters available for optimization of the toroidal contour with respect to power dispersal. Care must be taken, however, to choose parameter combinations which are compatible with the imposed gap between tiles. For fixed a_e,

b_e and R_{tile}, the half-angle subtended by the cylindrical part of the tile, ϕ, must be calculated based on the constraint of the minimum separation, d. For most cases, $\phi < \theta/4$ and the minimum distance is found between the two corners of neighbouring tiles where the straight line side segments intersect the tile base. A check must also be made to ensure that parameter combinations do not lead to a thickness at the thin part of the tile less than a specified value to avoid the tile becoming mechanically too fragile. For the design study described here, 4 mm is chosen for the minimum thickness of the *non-curved* part of the tile (the segment P_1P_2 in Fig. 2(b)).

3.2. Modelling the SOL power profile

Whilst the range of field line angles to be expected at the tile surfaces can be computed from magnetic equilibrium reconstructions of previous discharges (see later), there are currently no measurements of the main SOL heat flux widths, λ_q, in TCV. The optimum toroidal contour of criterion (a) above thus depends to a large extent on the validity of the assumed edge radial profiles and the model used to map these profiles onto the tile surface.

With regard to magnetic field line impact angles, Fig. 3 illustrates how the absolute value of the total magnetic field impact angle, α_t, along the central column at radius R_{tile}^{max} varies in the region close to that of the plasma–surface interaction for four of the equilibria shown in Fig. 1. For the configurations of Figs 3(a, b) limited on the central column, the total angle is zero at the point of contact of the LCFS where the radial component of the poloidal field, B_R, is zero. In contrast, for the case of the diverted configurations in Figs 3(c, d), α_t is largest at the upper strike point position where the poloidal field is almost purely radial and $B_z \approx 0$. From the point of view of power loading, such cases are of particular concern since, for SOL power profiles monotonically decreasing from the separatrix to larger radii, the highest power flux and the steepest impact angle coincide at the strike point.

It is clear that the model used to simulate the expected heat flux will depend on the nature of the configuration. Whilst identical SOL profiles can be imposed at some defined point on the equilibrium (e.g., on the low field side along a horizontal line passing through the magnetic axis, see later), the consequent power loading on the central column is somewhat easier to compute with confidence for a diverted discharge. In the latter case, the

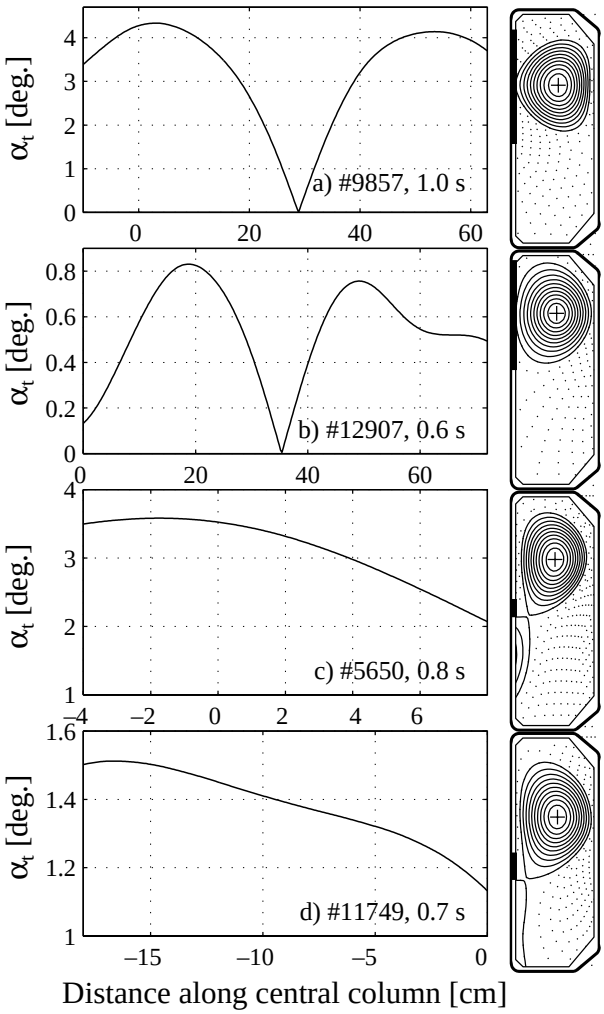

Figure 3. Dependence on vertical distance along the central column of the total impact angle, α_t, of magnetic field lines at $R = 0.624$ m for four of the example equilibria in Fig. 1 ($z = 0$ corresponds to the machine centre in cylindrical co-ordinates). The range of distance over which α_t is plotted is indicated by the bold vertical lines on the equilibrium reconstructions to the right of each plot.

plasma–surface interaction occurs at a single (per strike point) well defined location, whilst in the former (see, e.g., Fig. 1(b)) a large fraction of the column surface can be 'wetted' by the plasma. In this case, the fraction of the total input power, P_{IN}, arriving at the tile surfaces is more difficult to estimate. (A simple, but not necessarily accurate starting point would be to multiply P_{IN} by the ratio of the total plasma surface area to that in contact with the central column.) Although oblique incidence theoretically implies an absence of heat flux, measurements in tokamaks have shown that considerable heat and

particle fluxes [10, 11] can be transported across the magnetic field and hence be deposited on surfaces at glancing angle. In contrast, it has been found that a pure sine law describing the geometrical projection of heat flux onto target surfaces holds well for diverted discharges down to very low impact angles [12].

The highly localized nature of the strike point power flux, together with the relatively steep attack angles make for a credible worst case scenario in evaluating the optimum tile design. The diverted equilibrium in Fig. 1(c) is frequently employed for edge physics studies and has recently been utilized as a target plasma for observations of ECRH induced H mode transitions. In what follows, this configuration and, in particular, the inner strike zone with short poloidal connection length to the X point has been used extensively in the design of the new central column tiles.

To compute the power expected at the tile surfaces, a simple 1-D analytic model of the SOL has been adopted [13] in which heat enters the SOL via anomalous cross-field conduction and reaches the divertor according to classical conduction along open field lines connected to the target plates, where it is convected through the electrostatic sheath at the plate surface. This approach is commonly referred to as the 'two point' model, owing to the boundary conditions imposed at the 'symmetry point' — the point on field lines in the SOL equidistant between the two strike points (for a single null equilibrium) — and at the divertor targets. The model attempts to relate plasma parameters upstream of the divertor (i.e. at the symmetry point) with those in the target zones. These relationships depend on the extent to which parallel field temperature gradients can develop in the SOL, a phenomenon in turn dependent on the relative magnitudes of power reaching the edge plasma, the density there and the distance parallel to magnetic field lines between the symmetry point and the target zone.

For the case of TCV, the new tiles must be designed to withstand the power loads resulting from plasma heating with high power ECRH. The fully installed system will consist of 3 MW of X mode second harmonic heating at 82.6 GHz and 1.5 MW of X mode third harmonic heating at 118 GHz [4]. Whilst use at the third harmonic will permit heating at high densities, the cut-off density for the second harmonic system [14] is at $n_e = 4.3 \times 10^{19}$ m^{-3}, necessarily restricting experiments to rather low plasma densities with the potential for very high power densities (given the relatively small size of TCV). From the point of view of specifying likely edge conditions, high power ECRH at low densities implies high values of edge electron temperature, T_e, in the SOL and hence a low probability of parallel temperature gradients in the absence of forced edge cooling (e.g. by the injection of impurity gases to increase radiation losses). In this case, the edge plasma can be considered to be in the 'linear' or 'sheath limited' regime [13] with $T_d \cong T_s$ and $n_d \cong n_s/2$, where the subscripts s and d denote upstream (SOL) and divertor target, respectively, and where the factor of 2 in density is the result of flow acceleration from zero at the symmetry point to sonic at the target plate [15]. Under these conditions, the power flux density parallel to the field lines, q_s, in the SOL can be written simply as

$$q_s \sim q_d \sim \gamma n_s c_{sd} T_d \sim \frac{n_s \gamma T_s^{3/2}}{\sqrt{m_i/2}} \tag{1}$$

with $c_{sd} = \sqrt{2T_d/m_i}$ the ion acoustic speed at the target (assuming $T_i = T_e$), m_i the plasma ion mass, γ the sheath heat transmission factor describing the electron energy filtering efficiency of the electrostatic sheath at the target plates [15], and where the plasma temperature is written in energy units. In the absence of experimental measurements, q_s cannot be estimated using Eq. (1). Instead, a functional form for the radial decrease of parallel power flux in the edge at the symmetry point is imposed,

$$q_s(R_s) = q_{sep} \exp[-(R_s - R_{sep})/\lambda_q] \tag{2}$$

where λ_q is the characteristic length for the decay of power flux density in the SOL adjacent to the main plasma and where q_{sep} and R_{sep} are, respectively, the power flux density and major radius at the separatrix. A profile of this form is a direct consequence of Eq. (1) if $T_{e,i}$ and n_e decrease exponentially with radial distance in the SOL, a common observation in many tokamaks [15]. To compute $q_s(R_s)$ requires knowledge of both λ_q and q_{sep}. The approach here is to fix the total power, P_{SOL}, reaching the edge plasma and to assume that all of this power enters the SOL at the symmetry point. For a given λ_q, q_{sep} is then determined by matching P_{SOL} to the integrand of q_s across the SOL plasma and around the toroidal circumference.

The two point model is again useful in providing useful analytic estimates of λ_q in terms of machine parameters. For a non-circular single-null diverted configuration in the sheath limited regime, the following expression can be derived for the power

e-folding distance, assuming cross-field heat transport to be purely conductive [13]:

$$\lambda_q = 1.8\kappa^{1/10}\left(\frac{q_{95}}{\gamma}\right)^{2/5}(\chi_\perp R_0)^{3/5}\left(\frac{an_sm_i}{P_{SOL}}\right)^{1/5} \quad (3)$$

with κ the plasma elongation, R_0 the major radius, a the horizontal minor radius, q_{95} the safety factor on the 95% flux surface and $\chi_\perp$ the (anomalous) cross-field heat conduction coefficient. In practice, the latter cannot be measured directly in the SOL plasma and must be inferred from measurements of edge density and temperature profiles. Data are limited even in modern tokamaks and it is unclear how $\chi_\perp$ varies with plasma conditions and notably the different regimes of divertor operation. In general, estimated values lie in the approximate range 1–3 $\mathrm{m^2\,s^{-1}}$, but will depend, for example, on confinement mode, power into the SOL and plasma density [13].

With respect to the discharge in Fig. 1(c), for which $I_p = 280$ kA, $\kappa = 1.6$ and $q_{95} = 3.2$, Eq. (3) yields $\lambda_q = 2.6$ mm for $P_{SOL} = 2.5$ MW, $n_s = 1.4 \times 10^{19}$ $\mathrm{m^{-3}}$, $\gamma = 7$ and $\chi_\perp = 2.0$ $\mathrm{m^2\,s^{-1}}$. The chosen value of P_{SOL} assumes that from a maximum of 3 MW of X mode second harmonic ECRH, ≈15% will be lost by radiation and other processes. The contribution of ohmic heating to the total input power is assumed to be negligible in the presence of ECRH. The upstream density is taken to be a constant fraction of the central line averaged density, $n_s \approx \bar{n}_e/3$, as is frequently observed in tokamaks for a variety of confinement regimes [13]. For the same conditions but with $P_{SOL} = 1.0$ MW, Eq. (3) gives $\lambda_q \approx 3.0$ mm.

These rather low predicted values of λ_q are not inconsistent with the rather sparse experimental measurements reported in the literature [13], and are a simple consequence of the high SOL heating power specified at low density in a physically compact magnetic configuration. Despite the uncertainties and assumptions inherent in this approach to estimating the power e-folding length and in view of the absence of experimental measurements, the predictions of Eq. (3) are used here to determine the value of λ_q for the purposes of calculating expected tile surface power distributions.

3.3. Modelling the tile surface power distribution

The assumption of a sheath limited regime for the edge plasma means that the power conducted to the divertor strike zones can be obtained by mapping the midplane q_s profile to the divertor along magnetic flux surfaces. A method has been developed in which simple mapping of poloidal flux from the midplane to the central column is combined with a local analytic description of field line trajectories at the position of plasma–wall interaction. This approach permits rapid computation of the approximate expected surface power densities and, given the wide variation of possible plasma shapes in TCV, avoids the numerically intensive calculations necessary when following field lines in strongly shaped geometries.

To perform the mapping, the toroidal ring of poloidal flux at the outside midplane is first projected onto the cylinder of radius R_{tile}^{max}. The power flux density *perpendicular* to the column surface may then be written as

$$q_d = q_s \frac{R_s}{R_{tile}^{max}} \frac{dR_s}{d\psi_s} \frac{d\psi_d}{dz_d} \quad (4)$$

with $\psi_{s,d}$ the poloidal flux at each point in the midplane SOL and at the central column, respectively. Figure 4 shows the results of this flux surface mapping for two example equilibria (Figs 1(c, e)) and illustrates the differences to be expected in power deposition due to the differences in flux surfaces between limited and diverted configurations. In each case, the same exponential radial power profile for the parallel heat flux has been imposed at the outside midplane with $\lambda_q = 3.0$ mm and $P_{SOL} = 1.0$ MW. Radiation in the SOL has been neglected. It should be noted that in the case of diverted equilibria, no allowance is made in this simple model for perpendicular diffusion out of the SOL and into the divertor private flux region. In reality, such diffusion will lead to a 'rounding off' of the peak value, but for the case shown in Fig. 4 (discharge 11749), the extremely short connection length from X point to upper strike point will in any case limit the extent to which particles may diffuse from the SOL to the private flux zone during their transit to the target plate.

In Fig. 4, the power flux arriving at the central column has been computed by assuming, in addition to the simple description of an annular SOL, that the power flow may be divided equally between both strike points for the diverted equilibrium or wetted surfaces for the limited configuration. This will always be approximately true for many diverted equilibria, particularly for the ECRH target plasmas under consideration here for which the entire SOL will have the same low density and high temperature. Furthermore, for the class of discharges such as those

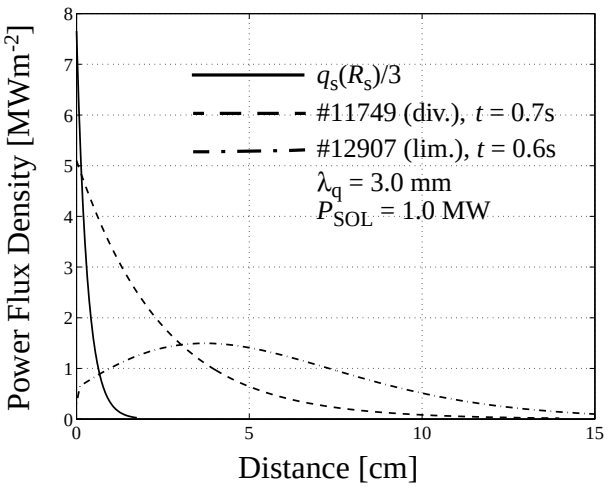

Figure 4. Dependence on vertical distance along the central column of the power flux density perpendicular to the tile surface for a perfectly cylindrical column with $R = 0.624$ m. Curves are computed for the inner strike zone of the equilibrium in Fig. 1(c) and the upper wetted area of the configuration in Fig. 1(e). The exponential power profile $q_s(R_s)$ imposed at the outside midplane is included for comparison (note the factor of 3 reduction for the purpose of plotting).

shown in Fig. 1(c), the magnetic connection lengths along the field from midplane to divertor targets are roughly equal (≈15 m for $I_p \approx 300$ kA) for both inner and outer strike points, so that strong power asymmetries would not be expected from the point of view of the magnetic geometry alone. Special drifts, such as those associated with edge toroidal rotation or parallel temperature gradients [16], which may lead to power asymmetries, are ignored. For limited discharges, the approximation probably also holds in general given the symmetry imposed by the central column acting in this case as an effectively continuous toroidal limiter.

The poloidal distributions of power flux density must now be imposed on a toroidally varying tile contour taking into account the local magnetic field line geometry. This procedure must account, of course, not only for the effect of the tile curvature itself in limiting the surface accessible to field lines, but also for the shadowing due to nearest neighbour tiles. A simple analytic description of the field lines in the tile vicinity can be obtained by requiring that the magnetic field components (B_R, B_z, B_φ) are constant along the field line connecting a point on the tile surface with the reference cylinder at radius R_{tile}^{max}. The cylindrical co-ordinates of any point along this field line may then be written as

$$\begin{pmatrix} R \\ z \\ \varphi \end{pmatrix} = \begin{pmatrix} R_{tile}^{max} \exp\left(\dfrac{B_R(z_R)}{B_\varphi} (\varphi - \varphi_R) \right) \\ z_R + R_{tile}^{max} \dfrac{B_z(z_R)}{B_\varphi} (\varphi - \varphi_R) \\ \varphi \end{pmatrix} \quad (5)$$

where (R_{tile}^{max}, z_R, φ_R) are the co-ordinates of its intersection with the reference cylinder and where the values of B_R and B_z are to be evaluated at R_{tile}^{max}. Equation (5) describes a helical trajectory with constant pitch in the z direction and a logarithmic spiral [17] in the plane (R, φ) with spiral constant equal to the ratio B_R/B_φ. For a point C on the tile linked to a point A on the projection cylinder (Fig. 5), solving the radial component of Eq. (4) for φ and substituing into the z component gives

$$\varphi_A = \varphi_C + \frac{B_\varphi}{B_R(z_A)} \ln\left(\frac{R_C}{R_{tile}^{max}} \right) \quad (6a)$$

and

$$z_A = z_C + R_{tile}^{max} \frac{B_z(z_A)}{B_R(z_A)} \ln\left(\frac{R_C}{R_{tile}^{max}} \right). \quad (6b)$$

Since the poloidal magnetic field components can vary considerably in moving vertically along the central column, the assumption of fixed B_R and B_z along any given field line will lead to a discrepancy between the computed and real impact points on the reference cylinder, particularly in the vertical direction. This will depend on both the radial distance between the tile surface and R_{tile}^{max} (at most ≈4.0 mm for the range of tile geometrical parameters studied here) and the ratio B_z/B_R. The latter depends sensitively on the type of configuration, being small at the upper strike point of diverted equilibria such as those in Figs 1(c, d) and large near the tangency point of limited discharges. Fortunately, in these latter cases, the field line attack angles are sufficiently low (Fig. 3) that regions with high tile curvature and hence the largest radial separations from the reference cylinder are shadowed from direct plasma impact (see later). Elsewhere, the radial separations are so small that the vertical displacement of a field line corresponding to its intersection with R_{tile}^{max} radius is rather small. For example, along the two plasma–surface interaction zones depicted in Fig. 4, this displacement for points on the tile surface accessible to field lines is at most 8 mm for the limited equilibrium and 3.5 mm for the diverted configuration (although this only

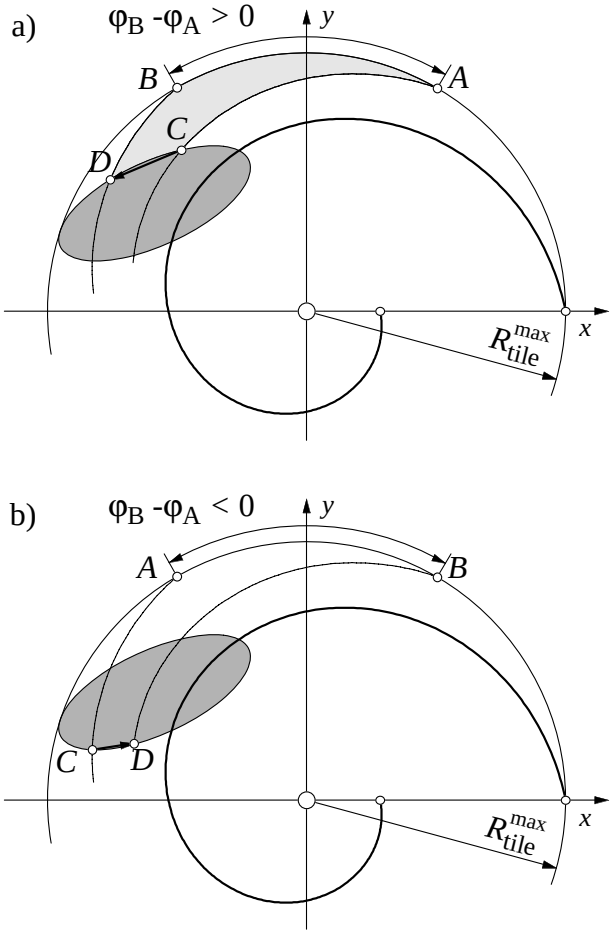

Figure 5. Two dimensional representation illustrating how the power deposition on an element of surface on the reference cylinder is mapped to the tile surface using magnetic field line trajectories described by logarithmic spirals. The tile itself (shaded region) is described by an arbitrary contour (showing that the method can be generalized to any shape) with greatly exaggerated curvature in order to render the spiral trajectories more obvious. In the vertical direction (z co-ordinate), the spirals have constant pitch. Shown are: (a) a non-shadowed tile contour element, $\varphi_B - \varphi_A > 0$; (b) a shadowed tile contour element, $\varphi_B - \varphi_A < 0$.

occurs far from the strike point where the power flux is in any case unimportant). Calculations in which the variation of poloidal flux across the tile surface itself is accounted for show the maximum error in the computed vertical displacement originating from the assumption of fixed B_R and B_z to be less than 10% for the limited discharge and negligible for the diverted equilibrium.

Using Eq. (6), a set of image points is easily generated on the reference cylinder and can thus be associated with a value of the perpendicular heat flux mapped from the midplane according to Eq. (4). The perpendicular heat flux deposited on the surface of the tile itself follows immediately from power balance by requiring that the heat inflow across a surface element on the reference cylinder be identical to the heat outflow over the corresponding element on the tile. This is illustrated graphically in Fig. 5(a) for a line segment $\overline{\mathrm{CD}}$ representing a small, arbitrarily chosen arc length on the tile contour. The points C and D map to the points A and B, respectively, at radius R_{tile}^{max}, and the heat flux over the surface bounded by the line segment is given by

$$q_{\overline{CD}} = q_{\overline{AB}} \left(\frac{R_{tile}^{max}(\varphi_B - \varphi_A) dz_{AB}}{|\boldsymbol{D} - \boldsymbol{C}| dz_{DC}} \right) \tag{7}$$

where dz_{CD} and dz_{AB} are, respectively, the lengths of vertical line segments bounding the surface elements on the tile and reference cylinder.

The final stage in the calculation is to account for tile curvature in preventing field lines accessing the tile surface, both for the case of self- and nearest-neighbour shadowing. The former is simply determined by the point at which the tangent to the tile contour is co-linear with the magnetic field line (neglecting Larmor radius effects). In the context of the example contour $\overline{\mathrm{CD}}$ above, for a smooth, convex contour such as those specified here, this point is equivalent to that at which $\varphi_B - \varphi_A = 0$ so that all the points with $\varphi_B - \varphi_A < 0$ are shadowed by the tile itself. This is illustrated in Fig. 5(b) where the field lines through C and D intersect the tile contour twice.

The shadowing effect of the tile on its nearest neighbour to the left (or counterclockwise) side can be deduced by symmetry arguments. Since $\varphi_B > \varphi_A$ when the heat flux can reach the tile and $\varphi_B < \varphi_A$ when it cannot, and since φ is maximum for the last counterclockwise point on each complete tile contour which can intercept a field line, it follows that no point on the neighbouring tile having a φ smaller than the largest value on the preceeding tile can receive power. Moreover, the rotational periodicity/symmetry of the central column tiles guarantees that the first φ for which field lines can access the left side nearest neighbour tile is equal to the first φ of the main tile minus $\theta/2$, where θ is the tile toroidal periodicity described in Section 3.1.

4. Choice of tile contour

Figure 4 illustrates how the steeper attack angles at the position of maximum power flux in diverted equilibria lead to higher power deposition than for limited discharges where the large flux expansion, and hence lower attack angles, help to spread the power. In seeking an appropriate toroidal tile contour, it is therefore pertinent to consider first those cases most likely to determine the power flux limits. These must also be equilibria frequently employed on TCV. A good candidate is the diverted discharge shown in Fig. 1(c) used thus far for illustrative purposes. A characteristic feature of this configuration (and most diverted discharges on TCV) is the short X point to central column distance. As mentioned earlier, there are limits to the extent of this separation owing to the requirements of vertical stability. In terms of tile design, increased distance in these types of equilibria implies lower flux expansion and hence higher power concentration. It turns out that at high ECRH power, very short flux expansion imposes a rather low limit on what could be tolerated for reasonable pulse lengths, however well the tile is optimized. One approach is therefore to choose an appropriate contour for a preferred equilibrium and provide estimates for what may be safely achieved for alternative configurations.

4.1. Power flux distribution at the tile surface

Using the local field line description in terms of logarithmic spirals developed in the previous section, the poloidal power flux distributions shown in Fig. 4 are numerically imposed on the parametric toroidal tile contour of Fig. 2(b). Assuming no Larmor radius effects and neglecting toroidal magnetic field ripple, the three tile parameters, a_e, b_e and R_{tile} are systematically varied through the range of values providing a realistic tile contour. The results are compiled in Fig. 6, where the power flux distribution along the toroidal tile contour is shown at the position of peak power deposition in the poloidal direction for each geometrical parameter combination. Each toroidal profile is plotted as a function of the angle subtended by the surface contour in the cylindrical co-ordinate system centred on the tokamak axis. As specified in Section 3.1, combinations of a_e, b_e and R_{tile} leading to a minimum tile thickness less than 4 mm are rejected, leading to the sparsity of cases at low R_{tile} with extreme tile curvature.

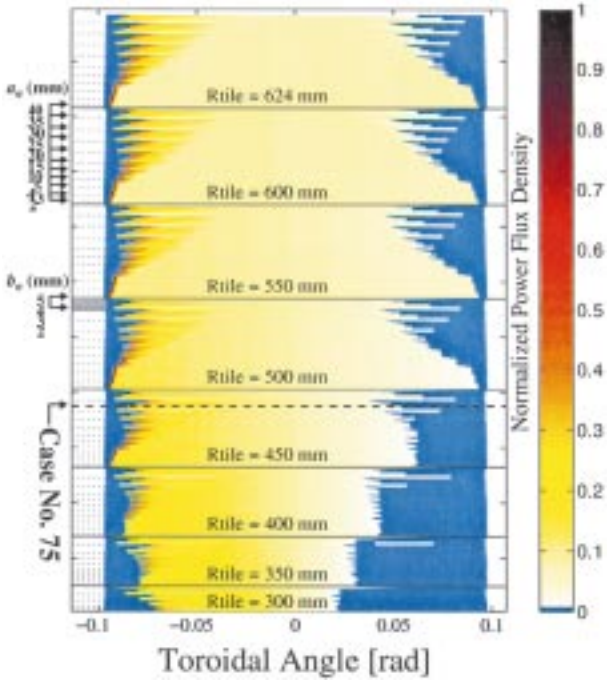

Figure 6. Normalized power deposition profiles along the tile toroidal contour at the poloidal location of maximum power for varying tile geometrical parameters and the model discharge of Fig. 1(c). Horizontal lines separate the tile radius groups and the light blue background designates zones in which no power is deposited due to nearest neighbour and self-shadowing. In each of the tile radius groups, dotted horizontal lines indicate the grouping in values of the ellipse major axis. The 'step-like' variation inside each group with fixed a_e is due to varying ellipse minor axis. Case number 75 is the toroidal contour chosen for the new column tiles (see text). The toroidal angle on the abscissa is the angle subtended by the curved tile surface in the cylindrical co-ordinate system centred on the tokamak axis.

For each simulated case, correct power accounting is verified by integrating the total deposited power on the tile surface and comparing with P_{SOL}. For reasonable choices of mesh size, agreement is generally within 1%. Although the profiles have each been obtained for $P_{SOL} = 1.0$ MW and $\lambda_q = 3.0$ mm (in accordance with Eq. (3)), normalizing the power in each case to the maximum power obtained for the ensemble of cases renders the choice rather arbitrary, with only the toroidal geometry being important. The effects of increasing R_{tile} and decreasing a_e in improving the tile wetted surface are evident, although this is at the expense of very highly localized power deposition at the tile extremities where field lines encounter almost vertical tile edges (up to

81.5 MW m^{-2}, even for relatively low P_{SOL}). Such cases cannot be considered as serious candidates for the optimum contour, which instead must provide for adequate power spreading and account for inevitable tile misalignments.

The choice of optimum toroidal contour is somewhat empirical and is based on inspection of the field line intersections with the tile surface along with the requirement for minimum peak heat flux, broadest deposition profile at peak and maximum wetted surface. As a qualitative measure of tile misalignment tolerance, the field line plots are inspected also for the case of a tile displaced radially inwards by 0.5 mm with respect to the nearest neighbour tile. This estimated maximum radial positional error between adjacent tiles is derived from measurements on the vacuum vessel following fabrication and is due to slight departures of the inner wall from a perfectly cylindrical surface. Additional positional errors due to departures from specified tolerances in tile and support rail thickness are of the order of a few 0.01 mm and considered negligible. No attempt has been made to account for cases in which the misalignment is not purely radial in character.

Of the 217 cases displayed in Fig. 6, those with $a_e \leq 10$ mm and $b_e \leq 3$ mm have excessively peaked power profiles and are rejected. Of the remaining 61 candidates, most are eliminated as a result of unacceptable power peaking or the low safety margin for field line impact on highly curved regions of the elliptical surface in the case of tile misalignment. Within the limitations of the simulations described here, there is little to choose between the handful of possible contours surviving the qualitative selection criteria. For the chosen magnetic field configuration, a contour with $R_{tile} = 600$ mm, $a_e = 40$ mm and $b_e = 5$ mm is little different with respect to power deposition than a tile with $R_{tile} = 450$ mm, $a_e = 35$ mm and $b_e = 4$ mm. Figure 7 illustrates the toroidal power deposition profile for the latter combination, chosen for the final design of the central column tiles, along with the field line intersection plot in the region of highest power deposition.

For a perfectly aligned tile, the peak power density is $P_{surf}^{max} = 24.8$ MW m^{-2} and the tile contour is such that field line impact cannot occur in areas of extreme curvature (or, equivalently, high impact angles), even in the case of a misaligned tile. In choosing a value for R_{tile} significantly smaller than R_{tile}^{max}, the tile curvature prevents field lines from impacting too near the highly curved regions at the ends of the elliptical section, whilst a high value of a_e provides

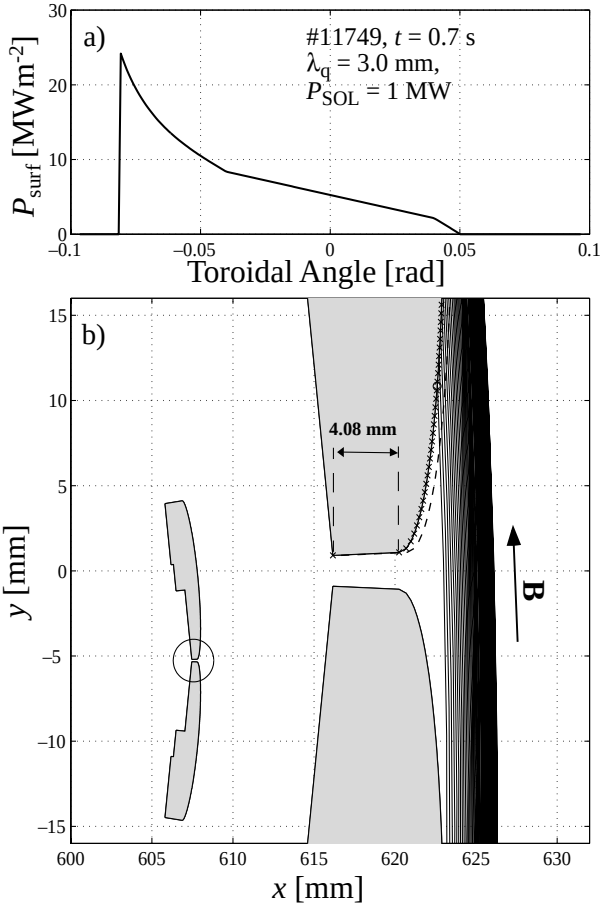

Figure 7. (a) Power deposition profile along the toroidal tile contour at the peak value of the poloidal power profile for a perfectly aligned tile. The curves correspond to case 75 in Fig. 6, with $R_{tile} = 450$ mm, $a_e = 35$ mm and $b_e = 4$ mm. (b) Close-up of two neighbouring tiles showing the first field line intersection point on the tile surface. The drawing illustrates the case for the thin half of each tile (Fig. 2) with the computed minimum thickness for this geometrical parameter combination indicated. The crosses mark the discrete points used to generate the tile contour, whilst the dashed contour corresponds to a tile misaligned by 0.5 mm purely in the radial direction.

for reduced impact angles at and near the first contact points. Higher values of R_{tile} have the advantage of a more uniform power deposition on the cylindrical part of the tile contour, but lead to slightly higher peak power values and a more discontinuous toroidal power profile at the join between cylindrical and elliptical regions.

In Fig. 8, full 2-D tile surface power distributions are shown for a tile with the chosen combination of geometrical parameters and for both the

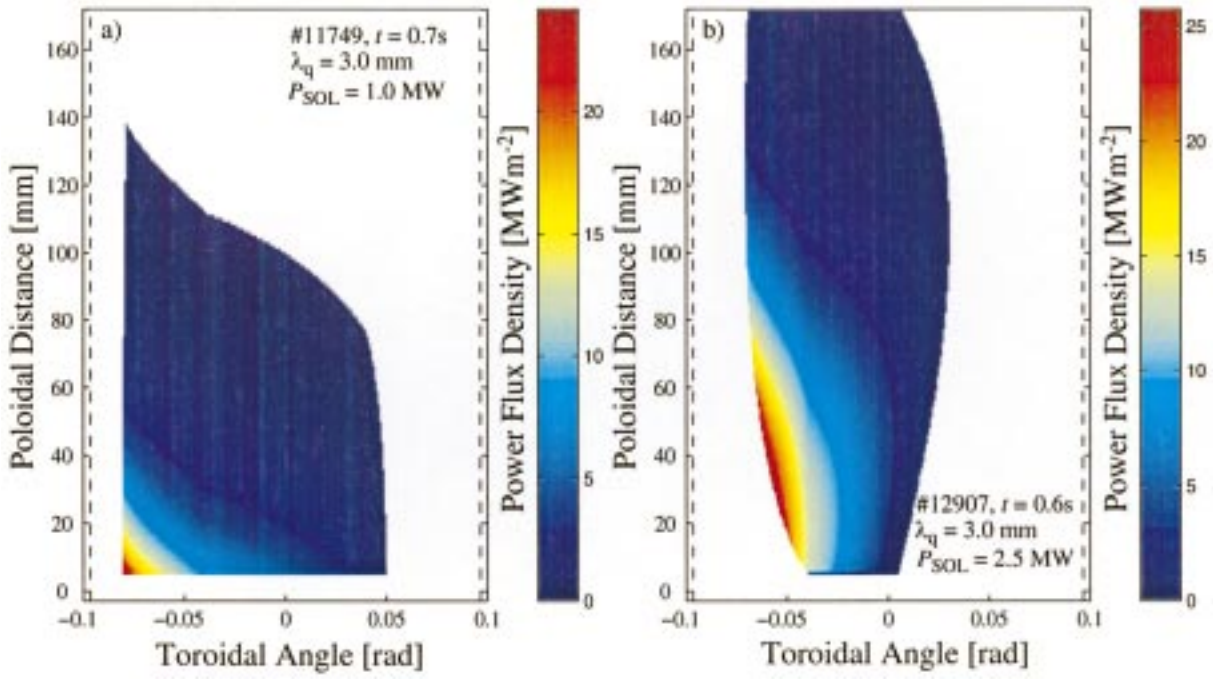

Figure 8. Computed surface power density distributions for (a) a diverted and (b) a limited equilibrium (Figs 1(c, e)) on a tile with contour given by $R_{tile} = 450$ mm, $a_e = 35$ mm and $b_e = 4$ mm and for $\lambda_q = 3.0$ mm. Note the factor of 2.5 increase in P_{SOL} for the limiter plasma in comparison with the diverted case. The vertical dashed lines show the position of the end points of the surface contour. All non-coloured areas to the left of each deposition pattern are zones in which field lines cannot access the tile owing to upstream nearest neighbour shadowing. Non-coloured zones to the right of each pattern are inaccessible due to tile self-shadowing.

diverted equilibrium on which the optimization was based and the upper wetted area of the limited discharge of Fig. 1(e), for which the poloidal power flux distribution at R_{tile}^{max} is also shown in Fig. 4. In both cases, the SOL power profile has been computed for $\lambda_q = 3.0$ mm, but P_{SOL} is increased to the maximum anticipated value for full power X mode second harmonic ECRH in the limiter case to illustrate the extent to which power handling is improved by the increased power spreading in comparison with the diverted discharge.

Figure 8(a) clearly shows the intense power localization at the bottom left corner of the tile where field lines at and near the separatrix with steepest angles impact the elliptical tile contour and where the maximum power fluxes flow. To be noted also is the well defined vertical border delimiting the power deposition to the left hand side of the tile and due to neglect of particle diffusion into the private region. In contrast, the limited plasma exhibits a much broader deposition profile with attack angles increasing away from the poloidal tangency point such that the maximum power deposition occurs closer to the tile centre where the curvature is reduced. For fixed λ_q, this allows the power entering the SOL to be increased by a factor of 2.5 to attain approximately the same peak power deposition ($P_{surf}^{max} = 26.6$ MW m^{-2}) as that for the diverted plasma. Although experimental confirmation of these computed deposition patterns can only be satisfactorily obtained using 2-D infrared camera measurements at the central column (in preparation at TCV), CCD TV observations of D_α recycling light in the tile vicinity indicate that the simulations closely reproduce the real spatial surface power distributions.

Whilst the details of what powers the tile may safely withstand from the thermo-mechanical point of view are discussed in Section 4.2, a general finding is that for the chosen graphite and heat pulse lengths of the order of 1 s, localized surface power fluxes must not exceed ≈30 MW m^{-2} if thermal sublimation limits are to be avoided. Both cases shown in Fig. 8 are thus close to thermal operational limits for the chosen values of λ_q and P_{SOL}. Depending on the magnitude of λ_q, a number of diverted equilibria possible in TCV must be excluded when high power levels are

required for long times. The discharge in Fig. 3(c) is a good example in which the low flux expansion at the upper strike point produces steep angles allowing field lines to access points further along the tile contour near the tile edges. This leads to extremely high power fluxes ($P_{surf}^{max} = 39.2$ MW m^{-2} for $\lambda_q = 3.0$ mm and $P_{SOL} = 1.0$ MW) and an unacceptable tile contour with regard to misalignment errors.

Allowing for all possible equilibria (many of which have not yet been created) results in a contour which unnecessarily restricts the tile surface area (and hence the permitted power deposition) exploited by the most frequently used configurations. Experiments must be performed with prudence using thermo-mechanical simulations as a guide to tolerable heat fluxes and complemented by measurements of λ_q and the distribution and absolute value of the power deposition itself. Such measurements are currently being planned at TCV. It is also clear that there is considerable latitude for reducing the modelled power deposition simply by choosing a larger value of λ_q for given P_{SOL}. Since the actual power scrape-off length may depend on a multitude of additional factors not explicitly incorporated into Eq. (3), the surface power distributions computed here serve as a simple basis from which extrapolations and comparisons with experiment can easily be made when measurements become available.

4.2. Finite element simulations

To investigate the thermo-mechanical compatibility of the chosen tile contour, 3-D finite element (FE) simulations using the ANSYS$^{\text{r}}$ software package (Release 5-4, ANSYS Inc.) have been performed including the full tile geometry. As before, the theoretically estimated power distributions of Fig. 8 will be used as representative of those expected in limited and diverted configurations in TCV, albeit at different P_{SOL}.

In order to correctly assess the ability of the tile to withstand the estimated power loads, tolerable mechanical and thermal limits must be imposed for the material in question. With regard to surface temperature, the maximum permissible value is taken to be that corresponding to the onset of radiation enhanced thermal sublimation of graphite due to ion impact. This effect, whilst identified in early, low fluence beam experiments as occurring at temperatures as low as ≈1400 K [18], is apparently not observed under the high ion flux densities characteristic of the tokamak edge, at least up to surface temperatures, T_{surf}, of about 2200 K [19]. For the purposes of this section, values of T_{surf} up to this limit will therefore be considered as tolerable in practice. Mechanical stress limits are determined using data supplied with each batch of machined tiles and through correspondance with the supplier. They are broadly limited to compressive and flexural stresses of less than 150 MPa and less than 65 MPa, respectively. The graphite selected for the new tiles is grade R6650MX2 from the SGL Carbon Group.[1]

The basic tile unit is modelled in three dimensions taking into account the asymmetric tile rear surface (in order to investigate the consequences of heat deposition on the thick and thin parts of the toroidal contour (Fig. 2(a)), but ignoring the machined volume for the tile mounting system (Fig. 12 in Section 5). Owing to the non-linear temperature dependence of the thermo-physical properties of graphite (the thermal capacity increases by a factor of 2.5 from room temperature to 1000 K and changes little thereafter, whilst the thermal conductivity decreases approximately exponentially with increasing temperature), the FE simulations include the temperature variation using data points obtained from the graphite supplier up to maximum temperatures of ≈2400 K. For comparative purposes, calculations have also been performed assuming average values of the thermal coefficients, both numerically with ANSYS, and analytically using standard expressions for the time variation of heat diffusion and stresses within a semi-infinite solid [20], in which the tile geometry is approximated by plates of finite thickness and infinite extension. Simulations are in all cases appropriate to heat pulse durations of 1 s and assume that peak heating occurs instantaneously. In making these calculations, proper energy accounting is rigorously ensured by comparing the theoretical energy deposited by the plasma model with that obtained by integration across the surface nodal heat flux matrix, and the thermal energy stored in the tile at the end of each load history. A more complete description of the FE results summarized here can be found in Ref. [21].

Figure 9 illustrates the FE computed surface temperature distributions at the end of a 1 s heat pulse with the power density distributions shown in Fig. 8 imposed, in this example, on the tile surface corresponding to the thin part of the toroidal contour. In

[1] SGL Carbon Group, Werk Ringsdorff, D-53170 Bonn, Germany.

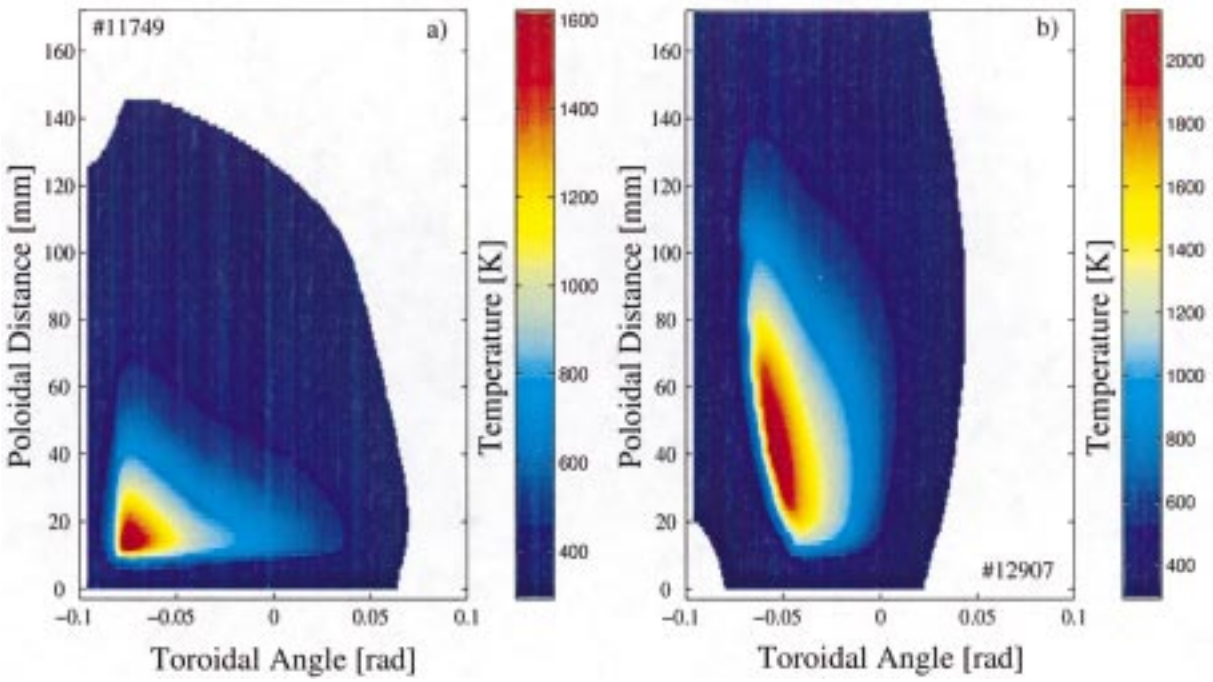

Figure 9. Surface temperature distributions from 3-D FE simulations of the tile response to the power densities of Fig. 8. Values are shown at the end of a 1 s heat pulse and have been computed taking into account the non-linear temperature dependence of the graphite thermal diffusivity. Results are shown for heat deposition on the thin half of the tile section. In case (a), the diverted plasma power distribution leads to $T_{surf}^{max} = 1630$ K for $P_{SOL} = 1.0$ MW, whilst in case (b) the limited equilibrium yields $T_{surf}^{max} = 2160$ K for $P_{SOL} = 2.5$ MW but with very similar values of peak power density.

the case of the limited plasma (Fig. 9(b)), the maximum attained surface temperature, $T_{surf}^{max} = 2160$ K, is somewhat higher than that for the diverted plasma with $T_{surf}^{max} = 1630$ K (Fig. 9(a)) and in both cases exceeds by only a few degrees the values found for heat deposition on the thick side of the toroidal contour. Calculations based on the assumption of semi-infinite solid behaviour or using ANSYS with a uniformly distributed heat flux and material coefficients independent of temperature compare well with each other but predict maximum temperatures several hundred degrees in excess of the FE method with non-linear coefficients. This is a consequence of the average thermal diffusivity being lower than the non-linear value below 1000 K.

Maximum compressive stresses of ≈100 MPa occur for power deposition on the thick side of the tile resulting from the limited plasma equilibrium and in the case in which the tile is assumed to be constrained with respect to movements perpendicular to the vacuum vessel support rail along its full length in the poloidal (or vertical) direction. Given that each tile is centrally fixed to the rail at a single point, this represents an upper limit to the compressive stress and is in any case only ≈66% of the maximum permitted value. Tensile stresses reach a peak value of 29 MPa (or 45% of the limit supplied by the manufacturer) for a tile constrained along its length and exposed on the thin side of the toroidal contour to the limited plasma configuration. These results compare favourably with those obtained from the semi-infinite, analytic and linear, uniformly heated FE solutions. For both compressive and tensile stress, the FE simulations show unequivocally that surface temperature is the restraining factor, at least for the examples of power distributions considered here.

The effect of temperature cycling is addressed in Fig. 10, illustrating the maximum nodal surface temperature from a non-linear FE simulation of four consecutive tokamak limiter discharges depositing the power distribution of Fig. 8(b) on the thin side of the tile contour for 1 s with 599 s idle time between discharges. Radiation from the tile front surface into the vacuum vessel, assumed fixed at ambient

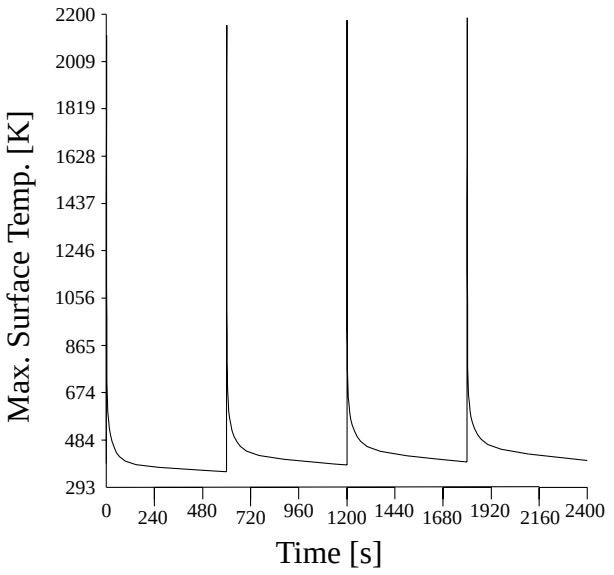

Figure 10. Time dependence of the maximum tile surface temperature for four simulated tokamak cycles comprising a 1 s discharge and 599 s idle time between discharges. The FE calculation includes heat loss by radiation from the tile front surface but no conduction from the back surface to the vacuum vessel. Results are appropriate to the computed 2-D power density distribution of Fig. 8(b) for the limited configuration of Fig. 1(e).

temperature, is included in the calculation leading to Fig. 10, although the correct value to assume for the surface emissivity is unknown. The latter depends on a variety of factors and may in particular be extremely sensitive to surface layers such as those deposited during tokamak operation or the regular vessel boronizations performed on TCV. On the basis of values measured by the supplier (SGL Carbon Group), a fixed value of 0.75 is assumed in order to establish a lower limit for the contribution of radiation to heat loss. After four cycles, $T_{surf}^{max} = 2185$ K and thermal equlibrium is reached after one further cycle. On the rear side of the tile, directly above the in-vessel magnetic probes, the temperature increases to a maximum of 564 K after four cycles. This is comparable with the typical first wall bakeout temperatures of ≈500 K in TCV. Radiation has little effect on the timescale of a single discharge, but is responsible for dissipating 35% of the total heat influx in the 600 s following the simulated power deposition. After four cycles, radiation loss has accounted for some 68% of the total energy deposited in the tile.

Owing principally to the absence of quantitative information describing the details of the thermal transfer from the graphite tile to the stainless steel support rail welded to the vacuum vessel wall, conduction losses have not yet been implemented in the FE model. Simple estimates based on a 100% contact area between the tile base and its support rail show that over a 600 s period, the tile may lose up to 30% of the initial stored energy.

Whilst the limited plasma of the TCV discharge of Fig. 1(e) is apparently permissible at maximum power for a 1 s discharge, the diverted configuration (and variants) of Fig. 1(c) will clearly lead to surface temperature limits being exceeded for full pulse duration at lower values of P_{SOL} (for given λ_q). The available latitude in pulse length is indicated in Fig. 11(a) where, for the surface power distribution of Fig. 8(a), the distribution has simply been renormalized to various values of P_{surf}^{max} and a new FE simulation performed for a single heating and cooldown cycle. The horizontal line at 2200 K marks the defined permitted value of T_{surf}^{max} and the points at which the rising portion of each curve cross the line determine the maximum time over which a heat pulse leading to the assumed values of P_{surf}^{max} could be safely applied. The imposed maximum power densities and corresponding times are assembled in Table 1. These values are of course specific to a given surface power distribution, or, equivalently, fixed λ_q. The pair of independent variables, P_{SOL} and λ_q, may be combined in many ways to produce a given value of P_{surf}^{max}. Figure 11(b) illustrates these combinations for each value of P_{surf}^{max} in Table 1 and has been generated by interpolation within a database of maximum surface powers compiled using an analytic formulation taking into account the fact that for the diverted discharge in question, the exponential power profile specified at the outer midplane remains exponential after magnetic mapping and leads to a divertor strike point profile broadened by a factor of 8 due to flux expansion.

Table 1. Permissible heat pulse durations before exceeding surface temperature limits for varying P_{surf}^{max} (TCV discharge 11749, $\lambda_q = 3.0$ mm)

P_{surf}^{max} (MW m^{-2})	t_{max} (s)
15	9.0
20	4.4
25	2.4
30	1.4
40	0.70
50	0.42

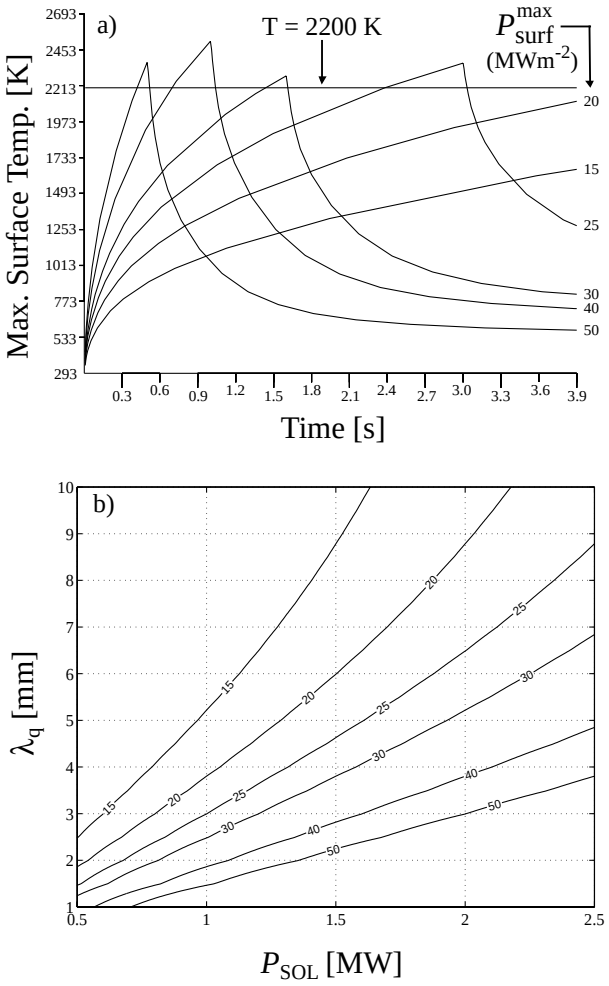

Figure 11. (a) ANSYS simulations showing the variation of heat pulse duration at given maximum surface power flux density before reaching a surface temperature of 2200 K. The curves are computed for the simulated power flux distribution of Fig. 8(a) corresponding to the diverted discharge of Fig. 1(c). In each case the distribution has been renormalized to the chosen values of P_{surf}^{max}. (b) For a fixed magnetic equilibrium, many combinations of P_{SOL} and λ_q can yield the same value of P_{surf}^{max}.

The same procedure can clearly be followed for any given plasma configuration but must be combined with full FE simulation of the surface power distribution in each case to yield the maximum times over which the heat pulse can be maintained. Returning to the diverted discharge for which the data are plotted in Fig. 11, if $P_{SOL} = 1.0$ MW leads to $P_{surf}^{max} = 25\ \mathrm{MW\,m^{-2}}$ at $\lambda_q = 3.0$ mm, then for fixed midplane profile shape, doubling P_{SOL} would lead to $P_{surf}^{max} = 50\ \mathrm{MW\,m^{-2}}$ and a maximum permissible heat pulse duration of just 420 ms. As is evident from Fig. 11(b), however, much longer discharge times would be possible for higher values of midplane power e-folding length (e.g. $t_{max} = 2.4$ s for $P_{SOL} = 2.5$ MW if $\lambda_q = 8.7$ mm). Given the multitude of possible magnetic equilibria together with the present lack of experimental information regarding λ_q on TCV, safe operating limits must be deduced from worst case estimates for each individual configuration.

5. Mechanical design and installation in TCV

A major obstacle for the design of protection elements for the TCV central column is the limited space available for the tile support and fixing system. For the tile design described in the previous sections, only 14 mm of graphite thickness can be used for the components used to attach the tile to rails welded to the vacuum vessel. This precludes the use of spring systems of various designs which are generally employed to maintain elastic preload during thermal cycling or other mechanical forces. The solution adopted is to take advantage of the differing thermoelastic properties of graphite, stainless steel and Nimonic to produce an assembly of components for which the required elastic preload is sustained over the foreseen operating temperature range. As shown in the composite Fig. 12, this is achieved through the use of a high strength, hollow, Nimonic[2] screw in combination with a stainless steel plate and tube assembly housed in a machined pocket in the centre of each tile. The screw is tightened via a small hole drilled in the tile front surface so that all metallic components are hidden from direct plasma–surface interaction.

For temperatures below ≈700 K, preload is maintained purely by elongation of the hollow screw and compression of the 8 mm thick, semicircular ledge of graphite surrounding the central screw hole. The small plate distributes the compression load over a wider surface to prevent localized over-stressing of the graphite, but the tube plays no role at low temperature. At higher temperatures, the increased thermal expansion of the screw compared with that of the graphite is compensated for by expansion of the tube such that preload is sustained. Owing to the small difference between the amount of thermal expansion and machining tolerances, care must be taken

[2] Nimonic alloy 80A, Wiggin Alloys Ltd, Holmer Road, HR4 9SL, UK.

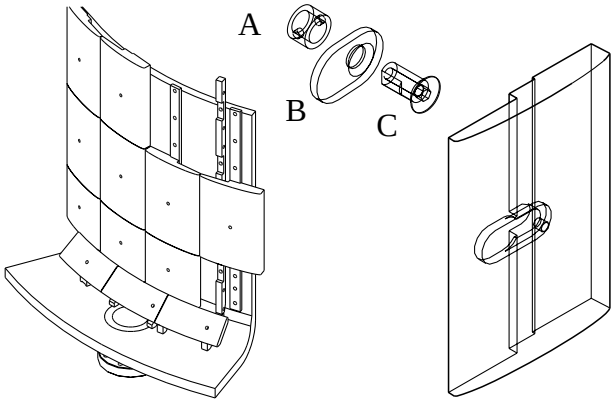

Figure 12. Illustration of how the new tiles cover the vacuum vessel central column (see also Fig. 13) and how individual tiles are fastened to rails welded to the vessel using a simple spring-free assembly comprising: A, stainless steel tube for thermal expansion compensation at high temperatures; B, stainless steel plate for reducing local stress on the graphite tile; C, hollow Nimonic fixing screw.

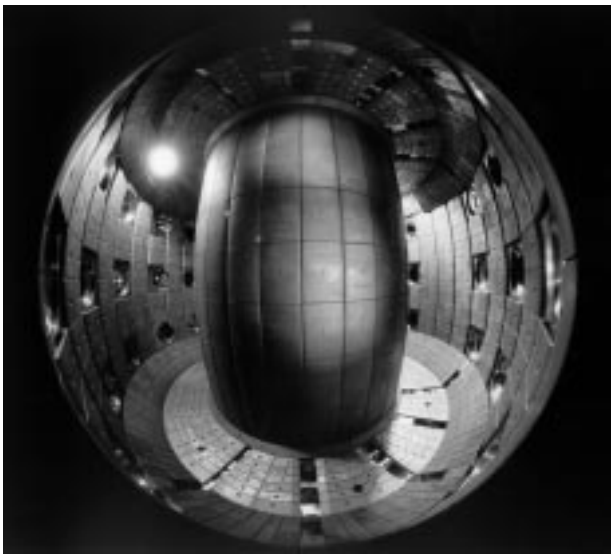

Figure 13. Vessel interior at the end of the 1997–1998 maintenance period following addition of the new central column tiles and outer wall protection.

in computing the required length of each component comprising the assembly [21].

The current status of first wall protection is shown in the photograph of Fig. 13, taken at the beginning of 1998, shortly after the installation of both the new tiles on the large major radius side of the vacuum vessel and the optimized central column tiles described in this article. At the time of writing, the number of individual graphite protection elements totals 1692, of which 288 constitute the new central column array. All tiles are machined in high purity, fine grain reactor grade graphites.

6. Summary

The addition of high power ECR heating capability on TCV has imposed an upgrade of the graphite protection armour, notably on the vacuum vessel central column used by the large majority of discharges as a limiter surface or divertor target zone. Protective components must satisfy the need for full toroidal symmetry, must be designed to tolerate power deposition resulting from a wide range of magnetic equilibria and must meet the tight space criteria imposed by vacuum vessel geometry and the requirement for passive wall stabilization at high elongation. Such constraints cannot be satisfied by a single tile design and the result of the optimization process described in this contribution is a compromise allowing tokamak operation at full second harmonic ECRH power for restricted heat pulse durations under the specific plasma conditions appropriate to its use (namely low plasma density) and dependent on the selected magnetic equilibrium.

A tile design has been chosen having a symmetric toroidal contour comprising cylindrical and elliptical sections and permitting parameterization in terms of three geometrical parameters which can be varied to yield acceptable power handling for a given magnetic geometry and the constraints imposed by inevitable tile misalignments. Computation of the expected 2-D surface power distribution for a given tile contour is performed by the combination of simplified poloidal magnetic flux mapping with an analytic approximation describing magnetic field line trajectories at near grazing incidence in the tile vicinity. Exponential profiles of power flux density specified by the total power conducted into the SOL, P_{SOL}, and the e-folding length of the edge power flow, λ_q, are imposed at the discharge midplane. The current absence of experimental information regarding λ_q on TCV leads to considerable latitude in the outcome of the simulations described here, particularly with respect to the peak power flux densities to be expected at the tile surfaces. Simple analytic estimates based on two point modelling of the diverted SOL are used as a guide in selecting an appropriate value of λ_q.

Surface power distributions have been computed for representative limited and diverted discharges typical of those employed in preliminary ECRH

experiments conducted before the central column tile upgrade and for fixed $\lambda_q = 3.0$ mm. Following the selection of a toroidal contour appropriate to both configurations, the thermo-mechanical response to the computed power fluxes has been investigated using 3-D FE simulations incorporating the non-linear temperature dependence of the graphite thermal diffusivity. The results indicate that full power operation for heat pulse durations of order 1 s will be safely possible for worst case limited plasmas, but that the considerably more peaked distributions at divertor strike zones will restrict pulse lengths if the small assumed value of the power e-folding length is appropriate. The real value of λ_q need not, however, be significantly greater for operation at full power and for the maximum envisaged pulse length of 2 s to be safely achieved. At the time of writing, a full set of central column tiles manufactured according to the design outlined in this article is installed and operating satisfactorily in TCV at current maximum ECRH power levels and pulse durations of 1.5 MW and 2.0 s, respectively. Operation at nominal full power of 3.0 MW is expected by late 1999.

Acknowledgements

This work was partly supported by the Swiss National Science Foundation. The authors are indebted to J.-M. Mayor for his invaluable assistance in preparing the technical design drawings for the graphite tiles.

References

[1] Mahdavi, M.A., et al., J. Nucl. Mater. **220–222** (1995) 13.
[2] Masaki, K., et al., J. Nucl. Mater. **220–222** (1995) 390.
[3] Hofmann, F., et al., Plasma Phys. Control. Fusion **36** (1994) B277.
[4] Goodman, T.P., et al., in Fusion Technology (Proc. 19th Symp. Lisbon, 1996), Vol. 1, Elsevier, Amsterdam and New York (1997) 565.
[5] Hofmann, F., et al., Nucl. Fusion **38** (1998) 399.
[6] Pochelon, A., et al., in Radio Frequency Heating and Current Drive in Fusion Devices (Proc. 2nd Eur. Conf. Brussels, 1998), Vol. 22A, European Physical Society, Geneva (1998) 253.
[7] Pitts, R.A., et al., J. Nucl. Mater. **241–243** (1997) 867.
[8] Weisen, H., et al., Plasma Phys. Control. Fusion **38** (1996) 1137.
[9] Chavan, R., et al., in Fusion Technology (Proc. 17th Symp. Rome, 1992), Vol. 1, North-Holland, Amsterdam (1992) 222.
[10] Pitcher, C.S., et al., J. Nucl. Mater. **196–198** (1992) 241.
[11] Seigneur, A., et al., in Controlled Fusion and Plasma Physics (Proc. 20th Eur. Conf. Lisbon, 1993), Vol. 17C, Part II, European Physical Society, Geneva (1993) 603.
[12] Matthews, G.F., Hill, D.N., Mahdavi, M.A., Nucl. Fusion **31** (1991) 1383.
[13] Pitcher, C.S., Stangeby, P.C., Plasma Phys. Control. Fusion **39** (1997) 779.
[14] Pochelon, A., et al., in Controlled Fusion and Plasma Physics (Proc. 20th Eur. Conf. Lisbon, 1993), Vol. 17C, Part III, European Physical Society, Geneva (1993) 1029.
[15] Stangeby, P.C., McCracken, G.M., Nucl. Fusion **30** (1990) 1225.
[16] Chankin, A.V., J. Nucl. Mater. **241–243** (1997) 199.
[17] Pearson, C.E., Handbook of Applied Mathematics, Van Nostrand Reinhold, Princeton, NJ, and New York (1974).
[18] Roth, J., Bohdansky, J., Wilson, K.L., J. Nucl. Mater. **111&112** (1982) 775.
[19] Philipps, V., et al., Nucl. Fusion **33** (1993) 953.
[20] Carslaw, H.S., Jaeger, J.C., Conduction of Heat in Solids, Oxford Science Publications, Oxford (1959).
[21] Chavan, R., CRPP Internal Rep. INT 195/99, Centre de Recherches en Physique des Plasmas, Lausanne (1999).

(Manuscript received 6 April 1999
Final manuscript accepted 11 August 1999)

E-mail address of R.A. Pitts:
richard.pitts@epfl.ch

Subject classification: B0, Td; I1, Td